



Almost 100 % electron transfer regime over Fe–Co dual-atom catalyst toward pollutants removal: Regulation of peroxymonosulfate adsorption mode

Fei Wang^{a,b}, Ya Gao^{a,b}, Huifen Fu^{a,b,*}, Shan-Shan Liu^{a,b}, Yuwei Wei^{a,b}, Peng Wang^{a,b}, Chen Zhao^{a,b}, Jian-Feng Wang^c, Chong-Chen Wang^{a,b,*}

^a Beijing Key Laboratory of Functional Materials for Building Structure and Environment Remediation, School of Environment and Energy Engineering, Beijing University of Civil Engineering and Architecture, Beijing 100044, China

^b Beijing Energy Conservation & Sustainable Urban and Rural Development Provincial and Ministry Co-construction Collaboration Innovation Center, Beijing University of Civil Engineering and Architecture, Beijing 100044, China

^c Institute of Analysis and Testing, Beijing Academy of Science and Technology (Beijing Center for Physical & Chemical Analysis), Beijing Engineering Research Center of Food Safety Analysis, Beijing 100089, China

ARTICLE INFO

Keywords:

Fe–Co dual-atom catalyst
Peroxymonosulfate
Adsorption mode
Coordination structure
Electron transfer pathway

ABSTRACT

Fe–Co dual-atom catalyst (FeCo–DAC) with FeCo–N₆ moiety anchored in the carbon skeleton is fabricated to achieve a nearly 100 % electron-transfer process (ETP) for high-efficient peroxymonosulfate (PMS) activation by regulating PMS adsorption mode. The introduction of the adjacent metal site markedly boosted the reaction kinetic of bisphenol A removal by 5–10 times. The Fe–Co dual-site optimized the adsorption mode of PMS, in which electron rearrangement of the adsorbed PMS* complex is enhanced with weak stretching of O–O bond, thus driving an exclusive selectivity for ETP pathway, as demonstrated via experiments and density functional theory (DFT) calculations. Moreover, ca. 75 % total organic carbon removal efficiency is achieved for the actual airport wastewater and the biodegradability (BOD₅/COD) is greatly improved from 0.13 mg/L to 0.3 mg/L. This work provides new inspiration for the construction of Fenton-like catalysts with 100 % ETP pathway from the perspective of finely regulating the PMS adsorption mode on catalyst.

1. Introduction

Peroxymonosulfate-based advanced oxidation processes (PMS-AOPs) have been extensively investigated in wastewater treatment for degrading various refractory organic pollutants [1–4]. Various radicals like sulfate radical (SO₄^{•−}), hydroxyl radical (•OH) and superoxide radical (O₂^{•−}) along with non-radicals like singlet oxygen (¹O₂), high-valent metal-oxo (HVMO) species and electron transfer process (ETP) have been reported to participate in the removal of target pollutants [5–9]. Notably, ETP has demonstrated some advantages like rapid pollutant removal, minimizing the toxic byproducts, lowering oxidant consumption, high tolerance to wide pH range and water matrix, which is deemed to advance the practical wastewater decontamination [10–12]. Nevertheless, the ETP pathway is usually accompanied with production of other reactive oxygen species (ROSS) like SO₄^{•−}, •OH,

¹O₂ and HVMO [13–16]. Although numerous ETP-dominated systems have been reported, most of them suffered from different ROSSs generation [17], in which the ETP selectivity is generally target-dependent (like rich-electron pollutants). Once such systems are employed in actual wastewater treatment, the alleged ETP selectivity would not work well as the co-existing substances like poor-electron pollutants would consume extra PMS via the radical pathway. Besides, the radical quenching resulting from the co-existing matters in the real water matrix would reduce PMS utilization efficiency and increase the operation cost [18,19]. From this point, the approach of switching a radical-involved process into a 100 % ETP pathway without other ROSSs formation is of great significance. However, there is no clear guidance reported for realizing the exclusive ETP pathway.

The formation of a PMS* surface complex via the adsorption-activation of PMS over functional catalysts is an initial and crucial

* Corresponding authors at: Beijing Key Laboratory of Functional Materials for Building Structure and Environment Remediation, School of Environment and Energy Engineering, Beijing University of Civil Engineering and Architecture, Beijing 100044, China.

E-mail addresses: fuhuifen@bucea.edu.cn (H. Fu), wangchongchen@bucea.edu.cn, chongchenwang@126.com (C.-C. Wang).

<https://doi.org/10.1016/j.apcatb.2023.123178>

Received 9 June 2023; Received in revised form 30 July 2023; Accepted 13 August 2023

Available online 14 August 2023

0926-3373/© 2023 Elsevier B.V. All rights reserved.

step for ETP pathway [20]. A great deal of reported catalysts generally referred to single-adsorption site of PMS through oxygen atom in peroxide bond. However, this adsorption mode would trigger O–O cleavage and inevitably produce various radicals [21–23]. In another single-site adsorption mode, the ended oxygen single-bonded with S adsorbed on catalysts easily facilitated the $\text{SO}_5^{\cdot-}$ and $^1\text{O}_2$ generation [6, 20, 24]. It seems difficult to accomplish an exclusive ETP pathway without other ROSs formation by individual active site. In principle, simultaneously guaranteeing the adequate-activation of PMS and avoiding the over-stretched of O–O bond are crucial to construct an efficient exclusive ETP pathway. Compared with the single-site adsorption, PMS adsorption occurred on a dual-site structure provides promising chance for intensifying charge rearrangement, regulating the length of the stretched O–O bond and thus controlling the desired activation pathway. Dual-atom catalysts (DACs) with two neighboring metal sites, perfectly inheriting the merits of single-atom catalysts (SACs), provide infinite possibilities for designing specific active sites by regulating the combination of different metals, metal-metal distance, geometric structure and electronic structure [25–27]. Wang's group found that Cu–Cu dual-atom catalyst with a suitable $d_{\text{Cu–Cu}}$ distance of 5 ~ 6 Å exhibited the greatly enhanced catalytic peroxydisulfate (PDS) activation performance via ETP because the two ended oxygen atoms of PDS matched well with the Cu–Cu distance to form a dual-site adsorption and activation mode [28]. Heteronuclear DACs with asymmetrical charge distribution might enabled the optimization of activity and selectivity feasible [29]. However, distinct oxidation mechanisms have been recently reported for the same DACs (e.g., Fe–Co DACs) [30–32], which deserve further in-depth exploration. Besides, to our best knowledge, the exclusive ETP-dominated oxidation system by regulating PMS adsorption mode over heteronuclear DACs has yet been reported.

Herein, we precisely constructed a heteronuclear Fe–Co dual-atom catalyst (FeCo–DAC) with a unique coordination configuration. The adjacent two metal sites achieved a dual-site adsorption of PMS, in which the two ended oxygen atoms double-bonding to S in PMS are adsorbed onto the neighboring Fe–Co dual-atom sites. The dual-site PMS adsorption mode averted the breakup of O–O bond, intensified the electron rearrangement and eventually drove a highly-selective and efficient ETP pathway almost without other ROSs generation. On the one hand, in the FeCo–DAC system, the ETP pathway contributed up to nearly 100 % for the BPA removal, while both radical and non-radical processes were involved in the corresponding monometallic Fe–SAC or Co–SAC counterparts. On the other hand, FeCo–DAC with the new FeCo–N₆ moiety greatly outperformed the Fe–SAC with Fe–N₄ moiety and Co–SAC with Co–N₃ moiety. Density functional theory (DFT) calculations are applied to discern the structure-activity relationship, especially to clarify the role of dual atomic pair in optimizing PMS adsorption mode, high-selective ETP pathway and high-efficient organics degradation. Moreover, FeCo–DAC achieves ca. 75 % total organic carbon (TOC) removal efficiency of actual airport wastewater and the biodegradability of treated airport wastewater is greatly enhanced. This study will provide further inspiration for designing exclusive an ETP-dominated catalytic process for actual wastewater treatment in the view of PMS adsorption mode.

2. Materials and methods

Details of the used chemicals reagents, characterization methods, DFT calculations and analysis methods are provided in [Supporting Information \(SI\)](#).

2.1. Preparation of ZnCo–ZIF@Fe(acac)₃, ZnCo–ZIF, Zn–ZIF@Fe(acac)₃ and ZIF–8

The synthesis procedures of ZnCo–ZIF@Fe(acac)₃ precursor were as follows. Briefly, 2.997 g of 2-methylimidazole, 2.022 g of Zn

(NO₃)₂·6H₂O, 0.066 g of Co(NO₃)₂·6H₂O and 0.0846 g of iron acetylacetonate (Fe(acac)₃) were dissolved in methanol under vigorous stirring at room temperature. After 24 h, ZnCo–ZIF@Fe(acac)₃ precursor was obtained by centrifugation, washing and drying.

ZnCo–ZIF and Zn–ZIF@Fe(acac)₃ were prepared by the similar procedure without the addition of Fe(acac)₃ and Co(NO₃)₂·6H₂O, respectively. Besides, ZIF–8 was synthesized without the introduction of Fe(acac)₃ as well as Co(NO₃)₂·6H₂O.

2.2. Preparation of FeCo–DAC, Co–SAC, Fe–SAC and N–doped carbon

ZnCo–ZIF@Fe(acac)₃, ZnCo–ZIF, Zn–ZIF@Fe(acac)₃ and ZIF–8 were respectively pyrolyzed at 900 °C for 2 h with the pyrolysis heating rate of 5 °C/min under N₂. After naturally cooled down to room temperature, the black powder was collected and labeled as FeCo–DAC, Co–SAC, Fe–SAC and N–doped carbon (N/C), respectively.

2.3. Catalysis test experiment

The PMS-AOP catalytic performances of the catalysts were evaluated for organic pollutants removal. The concentrations of targeted pollutants like bisphenol A (BPA), phenol (PN), rhodamine B (RhB), ofloxacin (OFC) and tetracycline (TC) were determined to be 20 mg/L. The catalytic PMS activation experiments were conducted in a PCX50C reactor (Beijing Perfect Light Technology Co., Ltd), in which the as-prepared FeCo–DAC catalyst (10.0 mg) was added to the targeted pollutants solution (50.0 mL) in a quartz reactor. After achieving the adsorption equilibrium, the reaction was initiated by the addition of 0.4 mM PMS. At fixed time interval, 1.0 mL solution was taken out and filtered via a 0.22 μm syringe filter and instantly quenched with 10.0 μL methanol for determination and analysis by high-performance liquid chromatography (Vanquish Duo). The detailed analysis methods were shown in [Table S1](#).

The concentrations of various inorganic ions and chemical oxygen demand (COD) in actual airport wastewater were exhibited in [Table S2](#). Owing to the high COD concentration of the original airport wastewater (excess 1000 mg/L), it was diluted by 20 times for the following experiments.

3. Results and discussion

3.1. Characterizations

The synthesis strategy of FeCo–DAC was illustrated in [Fig. 1a](#). A spatial encapsulation strategy was employed to encapsulate Fe(acac)₃ in the bimetallic MOF (ZnCo–ZIF) to prepare ZnCo–ZIF@Fe(acac)₃ precursor. The obtained ZnCo–ZIF@Fe(acac)₃ was then pyrolyzed to produce FeCo–DAC. Zn was vaporized during the pyrolysis process to alter the distance of neighboring Co atoms and provide more free nitrogen sites, thus effectively hindering the aggregation of Fe and Co species [33]. Zn–ZIF@Fe(acac)₃, ZnCo–ZIF and ZnCo–ZIF@Fe(acac)₃ showed similar powder X-ray diffraction (PXRD) patterns ([Fig. S1a](#)) and distinct dodecagon shape with a lateral size of ca. 300 nm ([Fig. S2](#)). Two broad characteristic peaks at around 26° and 44° corresponding to graphitic carbon were detected in PXRD patterns of the FeCo–DAC, Co–SAC and Fe–SAC ([Fig. S1b](#)) [34]. FeCo–DAC, Co–SAC and Fe–SAC retained the dodecahedral shape with smaller particle size and rougher surface compared to their precursors ([Fig. 1b and S3](#)). To clarify the feature of single Co and Fe atoms in FeCo–DAC, aberration-corrected high-angle annular dark-field scanning transmission electron microscopy (AC-HAADF-STEM) image was obtained. No obvious aggregation of Co and Fe atoms, but Fe–Co atomic pairs (marked by red circles) were observed to anchor throughout the whole carbon skeleton ([Fig. 1c](#)). The distances of Fe–Co dual atom pairs marked in the randomly selected regions of [Fig. 1d](#) were all close to ~2.93 Å, indicating the existence of Fe–Co dual atom pairs. Elemental mapping images of FeCo–DAC exhibited that Fe, Co, C, and N elements were well-distributed on the

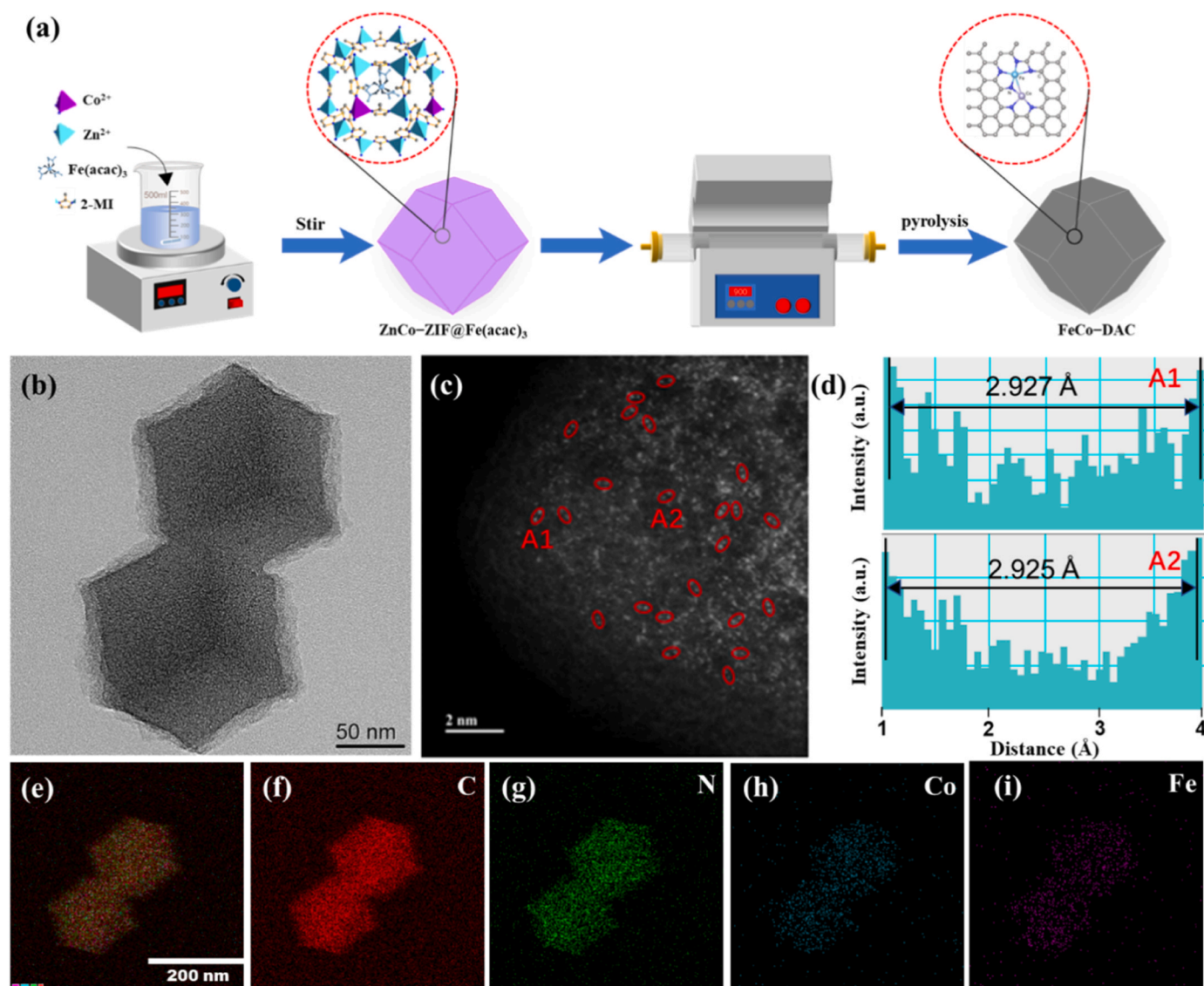


Fig. 1. (a) The preparation process of FeCo-DAC. (b) HRTEM, (c) AC-HAADF-STEM, (d) The corresponding intensity distributions for A1 and A2 regions in Fig. 1c, and (e–i) EDS mapping images of FeCo-DAC.

skeleton of carbon (Fig. 1e–i).

The contents of metal elements in the FeCo-DAC, Fe-SAC and Co-SAC were determined via inductively coupled plasma optical emission spectrometry (ICP-OES) (Table S3). The N 1 s XPS spectrum of FeCo-DAC could be fitted into four peaks situated at 398.4, 399.1, 400.1 and 401.3 eV corresponding to pyridinic-N, Co-N & Fe-N bonding, pyrrolic-N and graphitic-N, respectively (Fig. S4) [6]. Particularly, the introduction of Fe and Co resulted in a positive shift of various types of N, preliminarily indicating that N species have coordinated with Co and Fe [35]. In order to reveal the chemical state and the coordination environment of FeCo-DAC, Fe-SAC and Co-SAC catalysts, X-ray absorption spectra were conducted. The near-edge absorption of FeCo-DAC and Co-SAC at the Co K-edge was close to that of Co_3O_4 , and the absorption position was located between Co_3O_4 and Co foil, implying that the valence of Co element was between 0 and +8/3 (Fig. 2a) [20]. Similarly, the valence state of Fe atoms in FeCo-DAC and Fe-SAC was between 0 and +3 (Fig. 2d) [36].

To further determine the coordination mode of metallic atoms, the Fourier-transformed (FT) extended XAFS spectra were conducted. The solitary peaks at about 1.4 and 1.5 Å were attributed to the Co-N and Fe-N coordination bond in FeCo-DAC, respectively (Fig. 2b and 2e).

The absence of Co-Co coordination peak at 2.1 Å and Fe-Fe coordination peak at 2.2 Å suggested that the Fe-Co atomic pairs were atomically distributed throughout FeCo-DAC. The peak at around 2.5 Å assigned to Fe-Co bond in the Fe and Co K-edge FT-EXAFS spectra of FeCo-DAC and the distance of Fe and Co atoms well-matched with the AC-HAADF-STEM image results (Fig. 1c) further demonstrated the formation of Fe-Co atomic pairs. The coordination structure was verified as FeCo-N₆ owing to the well-fitted FT-EXAFS spectra on both the Fe and Co K-edge in FeCo-DAC (Fig. 2c, 2f, S5 and Table S4).

A maximum intensity at $\sim 4 \text{ Å}^{-1}$ was observed in the wavelet-transform (WT) plots of FeCo-DAC at the Fe and Co K-edge, which were ascribed to the Fe-N and Co-N bonds (Fig. 2g–i). Moreover, obvious characteristic signals of the Fe-Co bond were observed in the FeCo-DAC, whereas not detected for the Fe-SAC and Co-SAC (Fig. S6). Based on the above results, the presence of FeCo-N₆ moiety in FeCo-DAC was strongly confirmed. In addition, the calculated results obtained by least-squares fitting procedures revealed that the coordination number of Fe-N in Fe-SAC and Co-N in Co-SAC were 4.0 and 3.0, respectively (Fig. S7 and Table S4).

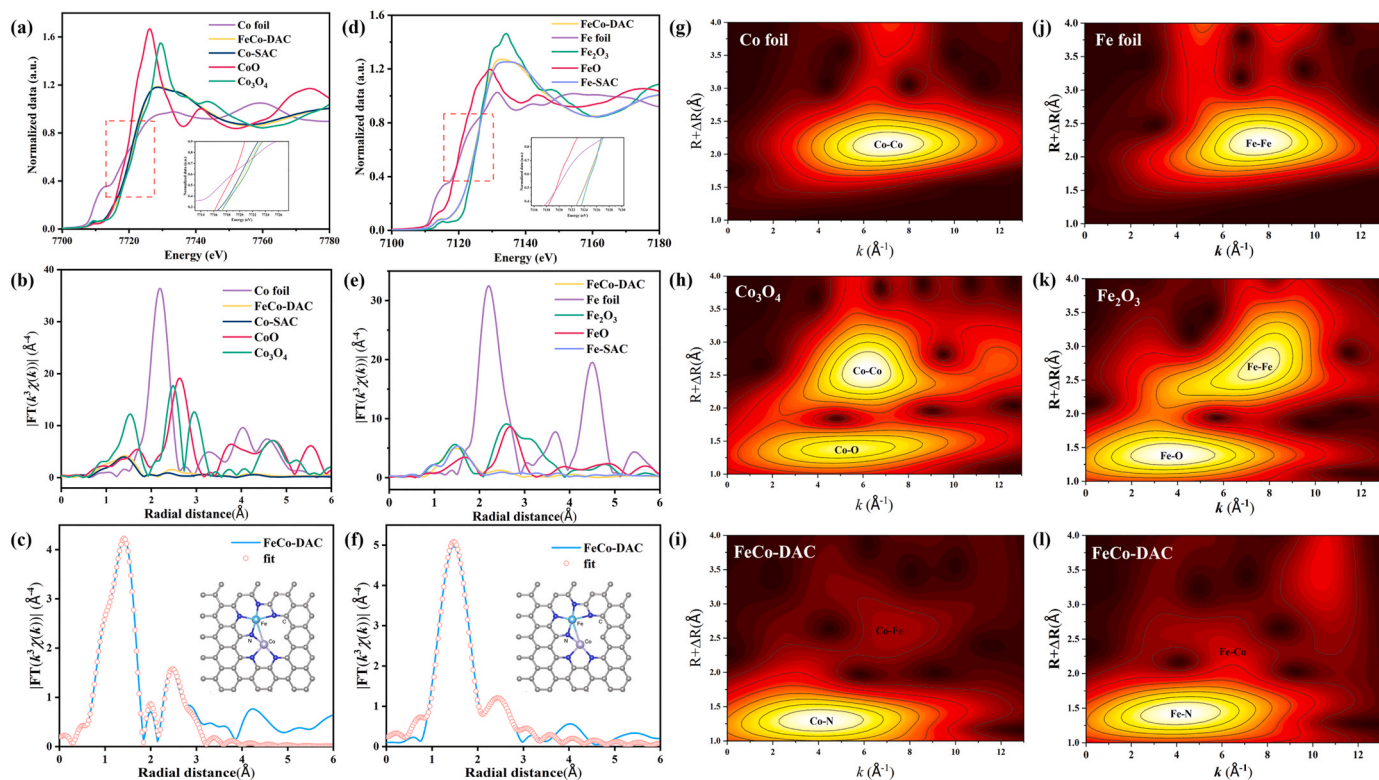


Fig. 2. XANES spectra at the (a) Co K-edge and (d) Fe K-edge of FeCo-DAC and reference samples. FT-EXAFS spectra at the (b) Co K-edge and (e) Fe K-edge of FeCo-DAC and their reference samples. EXAFS spectra fitting curves of FeCo-DAC at the (c) Co K-edge and (f) Fe K-edge (inset: structural model of FeCo-DAC). (g–l) WT of FeCo-DAC and reference samples.

3.2. Catalytic performance of the as-synthesized catalysts

The catalytic performances of as-synthesized catalysts were evaluated by PMS activation using BPA as a model pollutant. BPA removal was negligible in the presence of individual PMS and N/C. Ca. 69 % and 72 % removal efficiencies were achieved over the Fe-SAC and Co-SAC, respectively. As expected, FeCo-DAC exhibited the best catalytic performance, in which 100 % BPA was removed within 15 min (Fig. 3a). Meanwhile, FeCo-DAC achieved the higher BPA removal kinetics (Fig. S8a) (rate constant k of $\sim 0.23 \text{ min}^{-1}$) and TOC removal efficiency (Fig. S8b) (ca. 75 % within 15 min) compared to its corresponding monometallic catalysts. In addition, the toxicities of BPA and most of its intermediates were significantly reduced (Figs. S9 and S10). Particularly, the catalytic performance was enhanced obviously compared to the individual and physically mixed monometallic counterparts (Fig. S11), demonstrating the pivotal role of Fe–Co dual-atom pairs. The superior catalytic activities of FeCo-DAC were also found in the case of other recalcitrant pollutants like PN, RhB, OFC and TC (Fig. 3b). Considering the effect of reaction conditions on k , a modified kinetic model (k -value) was applied to evaluate the oxidation kinetics in different heterogeneous PMS-AOP systems [28,37]. The k -value of FeCo-DAC overpassed most of the state-of-the-art counterpart catalysts (Fig. 3c and Table 1).

BPA removal efficiency was improved with the increasing PMS dosage (Fig. S12a), and 98 % of PMS utilization efficiency was achieved, indicating that FeCo-DAC was a promising PMS activator (Fig. S12b). Fig. S13a illustrated that the initial solution pHs (1.0–11.0) exerted no obvious inhibition effect on BPA removal efficiency in FeCo-DAC/PMS system, demonstrating its wide pH application toleration. As shown in Fig. S13b, the influences of inorganic ions and humic acid (HA) on BPA degradation efficiency were investigated. Fortunately, the BPA degradation efficiencies were barely affected by some inorganic ions (F^- , NO_3^- , SO_4^{2-} and H_2PO_4^-) and humic acid (HA), with ca. 100 % removal

efficiencies of BPA being achieved. While the BPA degradation performance was obviously enhanced with addition of Cl^- and Br^- . This result demonstrated that Cl^- and Br^- could be rapidly oxidized into HOCl and HOBr to participate BPA degradation [71–74]. The above-mentioned results demonstrated that FeCo-DAC exhibited good practicability and anti-interference ability. A boosted BPA degradation performance was observed in actual simulated waterbody, especially tap water (Table S5 and Fig. S14) [75,76]. This was attributed to the high concentration of Cl^- in natural water like tap water, which promoted the BPA degradation (Fig. S15). Fig. S16 showed the TOC removal efficiency of real airport wastewater (the initial TOC concentration was 45 mg/L) in FeCo-DAC/PMS system, ca. 75 % TOC removal efficiency was achieved with the addition of 0.2 g/L FeCo-DAC and 0.4 mM PMS. Moreover, the biodegradability of real airport wastewater and treated real wastewater was investigated by determination of the ratio of BOD_5 and COD. The BOD_5/COD ratio was improved from 0.13 mg/L to 0.30 mg/L after treatment by activating PMS over FeCo-DAC, demonstrating that the biodegradability was enhanced. It could provide a basis for the subsequent coupled biological treatment.

FeCo-DAC also exhibited good reusability, only a slight decrease of BPA removal efficiency was observed after five cycles (Fig. S17a). This was mainly caused by the occupation of active sites by BPA intermediates, which was completely recovered via a heating treatment process (Fig. S17b) [77]. The iron and cobalt leaching concentrations were both below 0.10 mg/L (Fig. S17c), much lower than the drinking water standards [32]. Only 20 % BPA degradation could be accomplished by the PMS activation catalyzed by the dissolved Fe^{2+} and Co^{2+} ions with the identical concentrations of the leaching ones mentioned above, which ruled out the role of homogeneous system (Fig. S17d). Both the PXRD pattern and SEM image of used FeCo-DAC after the catalytic reaction maintained well, demonstrating its decent stability of FeCo-DAC (Fig. S18).

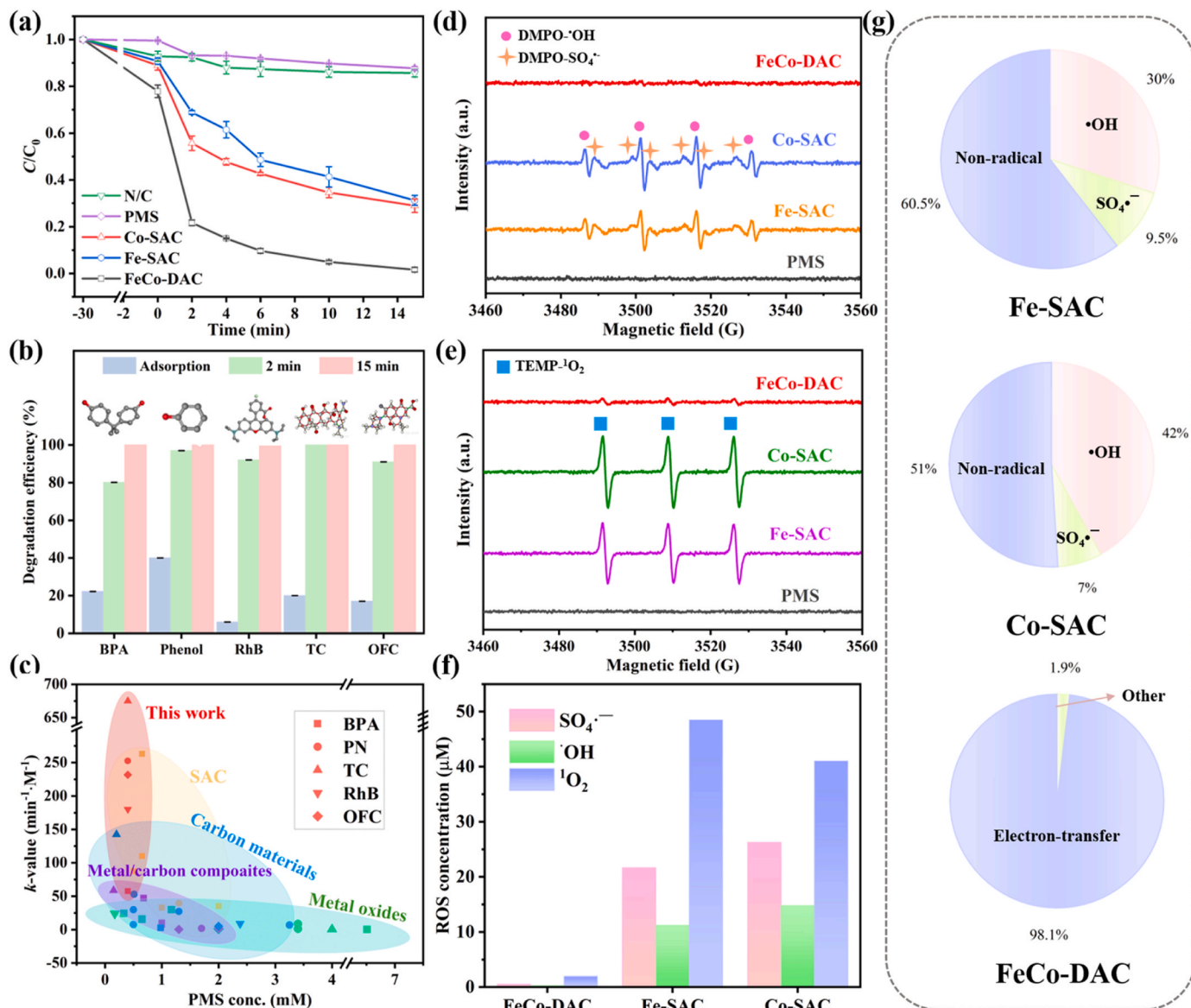


Fig. 3. (a) BPA degradation in different systems with addition 0.3 mM PMS. (b) Removal of multiple pollutants by FeCo-DAC catalyst and structures of the relevant pollutants (inset). (c) Comparison of k -value of pollutants degradation in different PMS-AOP systems. ESR spectra of (d) $\text{SO}_4^{\bullet-}$ and $\bullet\text{OH}$ and (e) $^1\text{O}_2$. (f) Quantitative determination of $\text{SO}_4^{\bullet-}$, $\bullet\text{OH}$ and $^1\text{O}_2$. (g) The contribution of various ROSs for BPA degradation in different oxidation systems. Reaction condition: catalyst = 0.2 g/L, PMS = 0.4 mM (except Fig. 3a), pH = 5.2, BPA = 20 mg/L, PN = 20 mg/L, RhB = 20 mg/L, TC = 20 mg/L, OFC = 20 mg/L.

3.3. Identification of reactive oxygen species

To identify the dominant ROSs, capture experiments and ESR measurement were conducted. As shown in Figs. S19a and 3d, the slight quenching by methanol (MeOH, quencher for $\text{SO}_4^{\bullet-}$ and $\bullet\text{OH}$) and undetectable ESR signals of $\text{DMPO-SO}_4^{\bullet-}$ and $\text{DMPO-}\bullet\text{OH}$ in FeCo-DAC/PMS system indicated that $\text{SO}_4^{\bullet-}$ and $\bullet\text{OH}$ played a negligible role in BPA degradation. Tert-butanol (TBA) brought about a slight inhibition, probably caused by the stronger affinity between TBA and FeCo-DAC due to the hydrophobic interaction [73]. No degradation of benzoic acid (BA), the typical radical probe for $\text{SO}_4^{\bullet-}$ and $\bullet\text{OH}$ [78,79], and undetectable $\text{SO}_4^{\bullet-}$ as well as $\bullet\text{OH}$ in FeCo-DAC/PMS system verified the absence of $\text{SO}_4^{\bullet-}$ and $\bullet\text{OH}$ (Figs. S19b, 3f and Table S6). Additionally, the ignorable inhibition by p-benzoquinone (BQ), extremely weak ESR signals of $\text{DMPO-O}_2^{\bullet-}$ and invisible $\text{O}_2^{\bullet-}$ signal at 560 nm detected by nitro blue tetrazolium (NBT) [80] proved the absence of $\text{O}_2^{\bullet-}$ (Fig. S21a–b). The above results ruled out the role of radicals on BPA degradation in FeCo-DAC/PMS system.

Slight quenching by DMSO implied the negligible contribution of HVMO (Fig. S21c). L-histidine was selected as the $^1\text{O}_2$ quenching agent [81]. The BPA degradation efficiency was slightly inhibited with the addition of L-histidine (Fig. S22a), which might be the direct reaction between PMS and L-histidine [82]. Furthermore, no enhanced BPA degradation by replacing H_2O with D_2O (Fig. S22b) and relatively weak ESR signal of $\text{TEMP-}^1\text{O}_2$ (Fig. 3e) excluded the role of $^1\text{O}_2$ in FeCo-DAC/PMS system [83].

Based on the above-discussed results, it was reasonable to speculate that ETP induced by catalyst-PMS* surface complexes might dominate the BPA degradation [12]. This hypothesis was further demonstrated by in-suit Raman spectra [84]. Besides the peak of HSO_5^- near 1061 cm^{-1} , a new peak (PMS*) was observed near 836 cm^{-1} after adding FeCo-DAC into PMS solution and disappeared after introduction of BPA (Fig. S23a) [85]. In this process, PMS was firstly adsorbed onto the FeCo-DAC surface to form PMS* by electronic rearrangement [28]. Then PMS* could capture electrons from BPA mediated by catalyst, leading to the BPA degradation and PMS decomposition into SO_4^{2-} .

Table 1

Comparison of the kinetics of organic contaminant degradation in recently reported PMS activation processes.

Catalyst (g/L)	PMS (mM)	Pollutants (mg/L)	Removal efficiency	k	k-value	Ref.
FeCo–DAC (0.2)	0.40	BPA (20)	100 % (15 min)	0.23	57.50	This work
CuFe ₂ O ₄ –Fe ₂ O ₃ (0.2)	1.17	BPA (5)	100 % (5 min)	1.41	30.13	[38]
DPA–hematite (0.5)	6.51	BPA (15)	100 % (120 min)	0.04	0.18	[39]
Co ₃ O ₄ –Bi ₂ O ₃ (0.3)	0.33	BPA (20)	98 % (30 min)	0.12	24.24	[40]
Mn _{1.8} Fe _{1.2} O ₄ (0.1)	0.65	BPA (10)	95 % (30 min)	0.10	15.38	[41]
Fe _{0.8} Co _{2.2} O ₄ (0.1)	0.65	BPA (20)	95 % (60 min)	0.05	16.13	[42]
O–C ₃ N ₄ (0.1)	10.0	BPA (12)	100 % (45 min)	0.065	0.74	[43]
Pd@g–C ₃ N ₄ (0.1)	1.0	BPA (20)	100 % (60 min)	0.038	7.60	[44]
10 %Ag/C ₃ N ₄ (0.1)	1.0	BPA (20)	100 % (60 min)	0.05	10.00	[45]
S–doped C ₃ N ₄ (0.1)	0.98	BPA (20)	80 % (120 min)	0.013	2.65	[46]
Fe ₈ A–N–C (0.15)	0.68	BPA (20)	100 % (15 min)	0.24	47.05	[47]
Fe ₁ /CN (0.5)	1.00	BPA (22.8)	100 % (10 min)	1.43	65.21	[48]
Cu–N ₄ /C–B (0.1)	0.65	BPA (20)	98 % (5 min)	0.56	172.31	[49]
Co–TPML (0.2)	2.00	BPA (11.4)	100 % (5 min)	2.40	68.40	[50]
Co–N/C (0.05)	0.50	BPA (10)	100 % (15 min)	0.352	140.80	[51]
Fe–Co–NC (0.1)	0.65	BPA (20)	100 % (4 min)	1.252	385.23	[52]
FeCo–DAC (0.2)	0.40	PN (20)	100 % (4 min)	1.01	252.50	This work
N–doped CNS (0.1)	3.25	PN (20)	97 % (120 min)	0.11	6.77	[34]
C–Mn (0.4)	1.70	PN (30)	100 % (90 min)	0.039	1.72	[53]
CPANI–9 (0.025)	0.50	PN (1)	100 % (10 min)	0.373	29.84	[54]
NoCNT–700 (0.1)	0.50	PN (20)	100 % (20 min)	0.2466	7.59	[55]
CeVO ₄ (1.0)	3.40	PN (100)	100 % (80 min)	0.0427	1.26	[56]
Co ₃ O ₄ –rGO (0.07)	3.40	PN (20)	100 % (~20 min)	0.1001	8.41	[57]
PAC (0.2)	1.30	PN (50)	100 % (15 min)	0.141	27.12	[58]
FeCo–N/C (0.05)	1.30	PN (15.3)	100 % (20 min)	0.316	74.38	[32]
FeCo–DAC (0.2)	0.40	TC (20)	100 % (2 min)	2.70	675.00	This work
CuCo@GCN–3 (0.1)	0.50	TC (20)	95.3 % (30 min)	0.182	72.80	[59]
Fe ₃ O ₄ @PANI–p 600 (0.4)	4.00	TC (20)	89.8 % (90 min)	0.0353	0.44	[60]
NPC–1100 (0.04)	0.20	TC (20)	100 % (60 min)	0.057	142.50	[61]
N–C/Co@PBS (0.4)	0.15	TC (10)	100 % (15 min)	0.3519	58.65	[62]
FeCo–DAC (0.2)	0.40	OFC (20)	100 % (6 min)	0.977	231.70	This work
0.4CF–Mt (0.4)	2.00	OFC (40)	85.2 % (60 min)	0.0261	1.31	[63]
5 %FeCu–g–C ₃ N ₄ (0.3)	0.30	OFC (10)	91 % (120 min)	0.0182	0.47	[64]
Co ₃ O ₄ /SnO ₂ (0.5)	2.00	OFC (20)	92 % (30 min)	0.049	0.98	[65]
BNC–0.5 (0.05)	0.51	OFC (40)	99.6 % (30 min)	0.045	52.94	[66]
Fe/CPC/TC–Mt–p (0.6)	2.00	OFC (40)	96.2 % (60 min)	0.0511	1.70	[67]
FeCo–DAC (0.2)	0.40	RhB (20)	100 % (10 min)	0.721	180.20	This work
α–MnO ₂ /Pal (0.1)	0.17	RhB (20)	100 % (180 min)	0.021	24.01	[68]
CoMn ₂ O ₄ /HACNFs (0.02)	1.00	RhB (24)	100 % (40 min)	0.093	111.60	[69]
NPC–800 (0.2)	2.38	RhB (100)	85 % (60 min)	0.042	2.38	[70]

Note: the modified kinetic rate constant (*k*-value) was calculated through dividing the observed rate constant of organic contaminants by the catalyst dosage and peroxide concentration, followed by multiplying organic contaminant concentration.

Chronoamperometry was conducted to further affirm the electron transfer process [12,86]. The significant current changes with addition of PMS (at ca. 200 s) and BPA (at ca. 300 s) indicated that the electron transfer occurred between FeCo–DAC and PMS (Fig. S23b). Besides, a remarkable increase of the current density in LSV curve in presence of FeCo–DAC, PMS and BPA, further demonstrated the presence of current flow (Fig. S23c) [87]. Considering that electron transfer regime would experience electron flow from pollutants to PMS and the oxidation process would happen without the involvement of ROSS [14,88], a premixing experiment was conducted to affirm that PMS and FeCo–DAC were first pre-mixed in the pure aqueous solution. The ignorable inhibition of BPA degradation implied that ETP was the dominant pathway (Fig. S23d). Moreover, FeCo–DAC–PMS* was confirmed to occur on the catalyst surface with electron transfer oxidation due to that the solution-phase scavengers of K₂Cr₂O₇ exerted almost no effect on BPA removal (Fig. S23e) [49]. These results demonstrated that the FeCo–DAC mediated ETP resulted from the reactive surface complexes (FeCo–DAC–PMS*) without producing free radicals, ¹O₂ and H₂O₂. In contrast, the combined (free radicals + non-radicals) processes were demonstrated to be indeed presented in Fe–SAC/PMS and Co–SAC/PMS systems on the basis of calculations of the relative contributions of ROSS for BPA degradation, quenching experiments and ESR analysis (Fig. 3d–g, S20 and S24) [5,24]. More importantly, the ETP contributed up to 98.1 % to BPA removal in the FeCo–DAC/PMS system, which might be attributed to the Fe–Co dual-site adsorption for

PMS of FeCo–DAC with the new FeCo–N₆ coordination structure.

3.4. DFT calculation for the PMS activation mechanism

To better understand the distinct catalytic behavior of Fe–SAC, Co–SAC and FeCo–DAC (Fig. S25), DFT calculations were conducted. PMS adsorption energy (*E*_{ads}), O–O bond length of PMS (*l*_{O–O}), and electron transfer tendency (*Q*) were calculated to reveal the origin of their different oxidation pathways [12,89]. As shown in Fig. 4a, PMS was adsorbed onto metal–N site by oxygen atom in peroxide bond for the Fe–SAC (Fe–N₄) and Co–SAC (Co–N₃), while a dual-site adsorption mode of PMS occurred in Fe–Co DAC (FeCo–N₆). Moreover, the *E*_{ads} of FeCo–N₆ was computed as –2.764 eV that was more negative than that of the Fe–N₄ (–1.811 eV) and Co–N₃ (–2.021 eV), indicating that the strongest affinity and relatively large electron transfer between PMS and FeCo–N₆ happened. Meanwhile, the PMS adsorption energies positively related to the reaction rate *k* and the turnover frequency (TOF) values of different catalysts (Fig. 4b). The *l*_{O–O} of adsorbed PMS was largely stretched in Fe–SAC/PMS (1.479 Å) and Co–SAC/PMS (1.484 Å) systems compared to FeCo–DAC/PMS system (1.472 Å), easily inducing the breakage of the O–O bond to generate radicals (SO₄^{•–} and •OH) [5], which was consistent with ESR results and radical quenching experiments. More importantly, the smallest *l*_{O–O} of FeCo–DAC/PMS could be attributed to the dual-site adsorption for PMS. To further clarify the electron transfer between PMS and catalysts (with FeCo–N₆, Fe–N₄ and

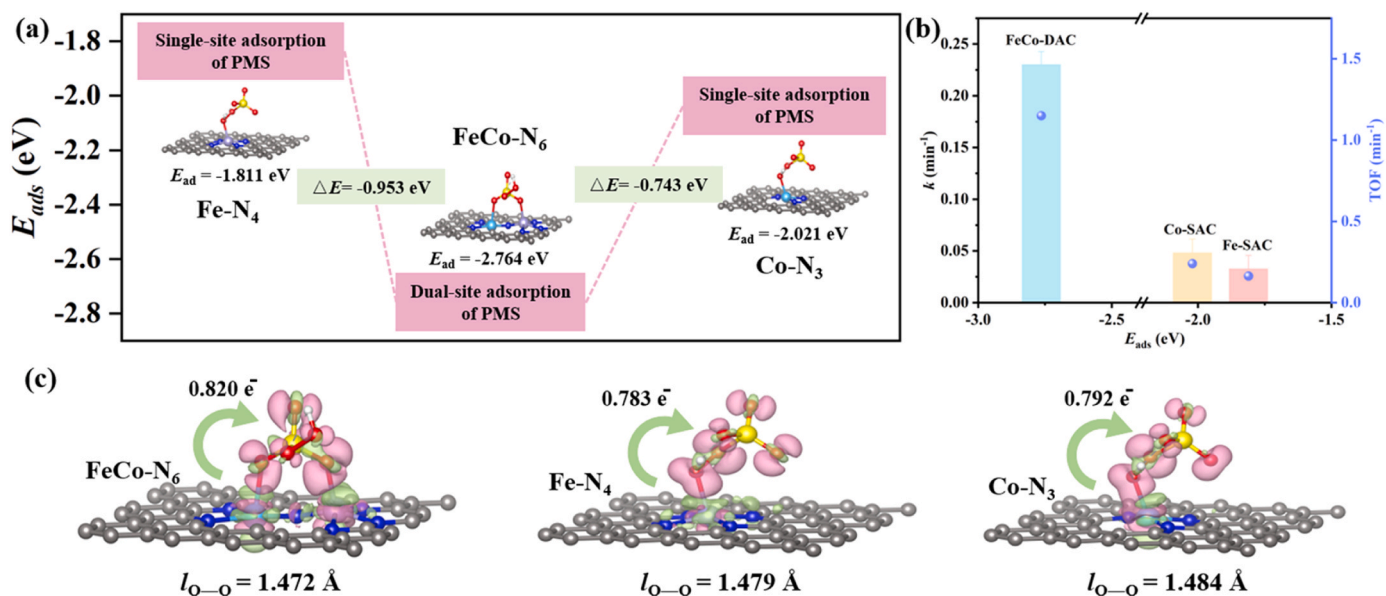


Fig. 4. (a) The calculated PMS adsorption energies on the FeCo-N₆, Fe-N₄ and Co-N₃ sites, the silver, cyan, gray, blue, yellow, red and white balls represent Co, Fe, C, N, S, O and H atoms, respectively. (b) The relationship between k and TOF values for different catalysts and PMS adsorption energy. (c) Electron density difference for PMS adsorption on FeCo-N₆, Fe-N₄ and Co-N₃ sites and the corresponding charge transfer and the length of O-O bond.

Co-N₃), the charge density difference analysis was calculated. Bader charge analysis showed that the electron transfer number from Fe-Co dual atom sites to PMS was $0.820 e^-$, which was much higher than those from Fe-N₄ ($0.783 e^-$) and Co-N₃ ($0.792 e^-$) (Fig. 4c). The enhanced charge transfer led to a more remarkable rearrangement of electrons between FeCo-N₆ and PMS, leading to high-efficient FeCo-DAC-PMS* complexes for rapid removal of BPA.

Based on the computational and experimental results, the adsorption mode and binding sites of PMS on catalyst greatly affect the electron rearrangement and charge distribution of PMS*. FeCo-N₆ in FeCo-DAC facilitated a larger electron transfer as well as more adequate activation of PMS with finite stretched of O-O bond due to its dual-metal site structure (Fig. 4a). While Fe-N₄ and Co-N₃ in the single-metal catalysts favored less electron transfer and more stretched O-O bond caused by the individual metal-N site for PMS adsorption (Fig. 4a). This distinct behavior triggered by different coordination configurations brought about distinct catalytic mechanisms: nearly 100 % ETP for FeCo-DAC, while a radical-nonradical combined process for its monometallic Fe-SAC or Co-SAC counterparts.

By constructing FeCo-DAC with dual-atom sites and precisely regulating the coordination mode of metal-N from Fe-N₄ and Co-N₃ to FeCo-N₆ and PMS adsorption mode from single-site adsorption (adsorption of oxygen atoms from peroxide bonds in PMS) to dual-site adsorption (adsorption of two ended oxygen atoms double-bonded to S in PMS), the high efficiency conversion of free radical pathway to a nearly 100 % ETP pathway could be achieved, which realize the rapid and high-efficient degradation of BPA (Fig. 5).

4. Conclusion

This work elucidated that regulating PMS adsorption mode by dual-atom sites could induce an ETP pathway without production of other active species like different radicals, ¹O₂ and HVMO species. The FeCo-DAC with the new FeCo-N₆ moiety provided dual-site to optimize the PMS adsorption mode, resulting in a more intensified electron rearrangement but finitely prolonged O-O bond, and thus driving an exclusive ETP pathway along with great outperformed activity. As to Fe-SAC and Co-SAC, the individual metal-N sites initiated single-site PMS adsorption and the consequential O-O cleavage to achieve a combined pathway (radical + non-radical). In addition, FeCo-DAC

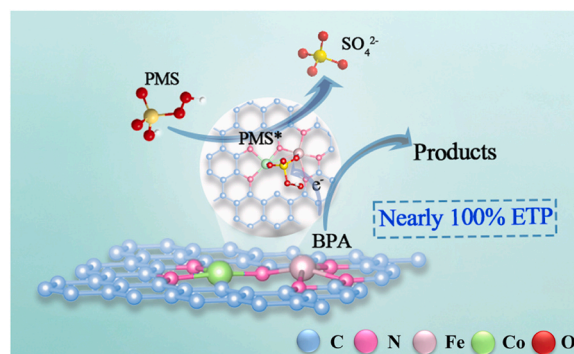


Fig. 5. The proposed mechanism for BPA removal in FeCo-DAC/PMS system.

exhibited outstanding degradation efficiency toward multiple refractory organic pollutants like BPA, PN, TC, OFC and RhB, in which 100 % removal efficiencies were accomplished in a wide pH range (1–11). FeCo-DAC also exhibited outstanding catalytic decomposition performance toward real airport wastewater, in which ca. 75 % TOC removal efficiency was achieved within 15 min with addition of FeCo-DAC (0.2 g/L) and PMS (0.4 mM). More importantly, the BOD₅/COD ratio was improved from 0.13 mg/L to 0.30 mg/L after being treated by PMS activation over FeCo-DAC, demonstrating that the biodegradability was enhanced. This work provided a new strategy for electron-transfer-based AOPs in pollutants removal, which inspired new ideas of catalyst design by regulating PMS adsorption mode to intentionally generate an exclusive ETP-dominated pathway for water decontamination.

CRedit authorship contribution statement

Fei Wang: Data curation, Investigation, Visualization, Software, Writing - Original draft preparation. **Ya Gao:** Data curation, Methodology. **Huifen Fu:** Conceptualization, Funding acquisition, Supervision, Project administration, Writing - review & editing. **Shan-Shan Liu:** Methodology. **Yuwei Wei:** Software. **Peng Wang:** Resources. **Chen Zhao:** Funding acquisition. **Jian-Feng Wang:** Resources. **Chong-Chen Wang:** Conceptualization, Funding acquisition, Supervision, Project

administration, Writing - review & editing.

Declaration of Competing Interest

The authors declare that they have no known competing financial interests or personal relationships that could have appeared to influence the work reported in this paper.

Data availability

Data will be made available on request.

Acknowledgements

This work was supported by National Natural Science Foundation of China (22176012, 51878023), Beijing Natural Science Foundation (8202016), The Project of Cultivation for young top-motch Talents of Beijing Municipal Institutions (BPHR202203079), R&D Program of Beijing Municipal Education Commission (KM202110016010, KM202310016007), Pyramid Talent Training Project of Beijing University (JDLJ20220802, JDYC20220817), BUCEA Doctor Graduate Scientific Research Ability Improvement Project (DG2023011) and the Cultivation project Funds for Beijing University of Civil Engineering and Architecture (X23034).

Appendix A. Supporting information

Supplementary data associated with this article can be found in the online version at [doi:10.1016/j.apcatb.2023.123178](https://doi.org/10.1016/j.apcatb.2023.123178).

References

- [1] F. Wang, S.-S. Liu, Z. Feng, H. Fu, M. Wang, P. Wang, W. Liu, C.-C. Wang, High-efficient peroxymonosulfate activation for rapid atrazine degradation by FeS₂/MoS₂ derived from MIL-88A(Fe), *J. Hazard Mater.* 440 (2022), 129723.
- [2] Y. Zhuang, X. Wang, L. Zhang, Z. Kou, B. Shi, Confinement Fenton-like degradation of perfluorooctanoic acid by a three dimensional metal-free catalyst derived from waste, *Appl. Catal. B: Environ.* 275 (2020), 119101.
- [3] Y. Zhuang, Q. Liu, Y. Kong, C. Shen, H. Hao, D.D. Dionysiou, B. Shi, Enhanced antibiotic removal through a dual-reaction-center Fenton-like process in 3D graphene based hydrogels, *Environ. Sci.: Nano* 6 (2019) 388–398.
- [4] H. Fu, C.-C. Wang, W. Liu, MOFs for water purification, *Chin. Chem. Lett.* 33 (2022) 1647–1649.
- [5] M. Yang, Z. Hou, X. Zhang, B. Gao, Y. Li, Y. Shang, Q. Yue, X. Duan, X. Xu, Unveiling the origins of selective oxidation in single-atom catalysis via Co–N₄-C intensified radical and nonradical pathways, *Environ. Sci. Technol.* 56 (2022) 11635–11645.
- [6] Y. Yao, C. Wang, X. Yan, H. Zhang, C. Xiao, J. Qi, Z. Zhu, Y. Zhou, X. Sun, X. Duan, J. Li, Rational regulation of Co–N–C coordination for high-efficiency generation of ¹O₂ toward nearly 100% selective degradation of organic pollutants, *Environ. Sci. Technol.* 56 (2022) 8833–8843.
- [7] J. Yang, D. Zeng, Q. Zhang, R. Cui, M. Hassan, L. Dong, J. Li, Y. He, Single Mn atom anchored on N-doped porous carbon as highly efficient Fenton-like catalyst for the degradation of organic contaminants, *Appl. Catal. B: Environ.* 279 (2020), 119363.
- [8] F. Wang, Y. Gao, S.-S. Liu, X.-H. Yi, C.-C. Wang, H. Fu, Fabrication strategies of metal–organic frameworks derivatives for catalytic aqueous pollutants elimination, *Chem. Eng. J.* 463 (2023), 142466.
- [9] Q. Zhao, C.-C. Wang, P. Wang, Effective norfloxacin elimination via photo-Fenton process over the MIL-101(Fe)-NH₂ immobilized on α-Al₂O₃ sheet, *Chin. Chem. Lett.* 33 (2022) 4828–4833.
- [10] Y.-J. Zhang, G.-X. Huang, L.R. Winter, J.-J. Chen, L. Tian, S.-C. Mei, Z. Zhang, F. Chen, Z.-Y. Guo, R. Ji, Y.-Z. You, W.-W. Li, X.-W. Liu, H.-Q. Yu, M. Elimelech, Simultaneous nanocatalytic surface activation of pollutants and oxidants for highly efficient water decontamination, *Nat. Commun.* 13 (2022) 3005.
- [11] Z. Zhou, M. Li, Y. Zhang, L. Kong, V.F. Smith, M. Zhang, A.J. Gulbrandson, G. H. Waller, F. Lin, X. Liu, D.P. Durkin, H. Chen, D. Shuai, Fe–Fe double-atom catalysts for murine coronavirus disinfection: nonradical activation of peroxides and mechanisms of virus inactivation, *Environ. Sci. Technol.* 57 (2023) 3804–3816.
- [12] W. Ren, C. Cheng, P. Shao, X. Luo, H. Zhang, S. Wang, X. Duan, Origins of electron-transfer regime in persulfate-based nonradical oxidation processes, *Environ. Sci. Technol.* 56 (2022) 78–97.
- [13] Z. Wang, J. Jiang, S. Pang, Y. Zhou, C. Guan, Y. Gao, J. Li, Y. Yang, W. Qiu, C. Jiang, Is sulfate radical really generated from peroxydisulfate activated by iron (II) for environmental decontamination? *Environ. Sci. Technol.* 52 (2018) 11276–11284.
- [14] E.-T. Yun, J.H. Lee, J. Kim, H.-D. Park, J. Lee, Identifying the nonradical mechanism in the peroxymonosulfate activation process: singlet oxygenation versus mediated electron transfer, *Environ. Sci. Technol.* 52 (2018) 7032–7042.
- [15] P. Shao, Y. Jing, X. Duan, H. Lin, L. Yang, W. Ren, F. Deng, B. Li, X. Luo, S. Wang, Revisiting the graphitized nanodiamond-mediated activation of peroxymonosulfate: singlet oxygenation versus electron transfer, *Environ. Sci. Technol.* 55 (2021) 16078–16087.
- [16] H. Li, Z. Zhao, J. Qian, B. Pan, Are free radicals the primary reactive species in Co (II)-mediated activation of peroxymonosulfate? New evidence for the role of the Co (II)–peroxymonosulfate complex, *Environ. Sci. Technol.* 55 (2021) 6397–6406.
- [17] Y.-H. Li, C.-C. Wang, F. Wang, W. Liu, L. Chen, C. Zhao, H. Fu, P. Wang, X. Duan, Nearly zero peroxydisulfate consumption for persistent aqueous organic pollutants degradation via nonradical processes supported by in-situ sulfate radical regeneration in defective MIL-88B(Fe), *Appl. Catal. B: Environ.* 331 (2023), 122699.
- [18] Y. Wei, J. Miao, J. Ge, J. Lang, C. Yu, L. Zhang, P.J.J. Alvarez, M. Long, Ultrahigh peroxymonosulfate utilization efficiency over CuO nanosheets via heterogeneous Cu(III) formation and preferential electron transfer during degradation of phenols, *Environ. Sci. Technol.* 56 (2022) 8984–8992.
- [19] F.-X. Wang, Z.-C. Zhang, C.-C. Wang, Selective oxidation of aqueous organic pollutants over MOFs-based catalysts: a mini review, *Chem. Eng. J.* 459 (2023), 141538.
- [20] X. Mi, P. Wang, S. Xu, L. Su, H. Zhong, H. Wang, Y. Li, S. Zhan, Almost 100% peroxymonosulfate conversion to singlet oxygen on single-atom CoN₂₋₂ sites, *Angew. Chem. Int. Ed.* 60 (2021) 4588–4593.
- [21] Z. Wang, J. Bao, H. He, S. Mukherji, L. Luo, J. Du, Single-Atom iron catalyst activating peroxydisulfate for efficient organic contaminant degradation relying on electron transfer, *Chem. Eng. J.* 458 (2023), 141513.
- [22] Q. Chen, Y. Liu, Y. Lu, Y. Hou, X. Zhang, W. Shi, Y. Huang, Atomically dispersed Fe/Bi dual active sites single-atom nanozymes for cascade catalysis and peroxymonosulfate activation to degrade dyes, *J. Hazard Mater.* 422 (2022), 126929.
- [23] Y. Guan, G. Fu, Q. Wang, S. Ma, Y. Yang, B. Xin, J. Zhang, J. Wu, T. Yao, Fe, Co, N co-doped hollow carbon capsules as a full pH range catalyst for pollutant degradation via a non-radical path in Fenton-like reaction, *Sep. Purif. Technol.* 299 (2022), 121699.
- [24] P. Yang, Y. Long, W. Huang, D. Liu, Single-atom copper embedded in two-dimensional MXene toward peroxymonosulfate activation to generate singlet oxygen with nearly 100% selectivity for enhanced Fenton-like reactions, *Appl. Catal. B: Environ.* 324 (2023), 122245.
- [25] Y. Yang, Y. Qian, H. Li, Z. Zhang, Y. Mu, D. Do, B. Zhou, J. Dong, W. Yan, Y. Qin, L. Fang, R. Feng, J. Zhou, P. Zhang, J. Dong, G. Yu, Y. Liu, X. Zhang, X. Fan, O-coordinated W-Mo dual-atom catalyst for pH-universal electrocatalytic hydrogen evolution, *Sci. Adv.*, 6 eaba6586.
- [26] W. Zhang, Y. Chao, W. Zhang, J. Zhou, F. Lv, K. Wang, F. Lin, H. Luo, J. Li, M. Tong, E. Wang, S. Guo, Emerging dual-atomic-site catalysts for efficient energy catalysis, *Adv. Mater.* 33 (2021) 2102576.
- [27] R. Li, D. Wang, Superiority of dual-atom catalysts in electrocatalysis: one step further than single-atom catalysts, *Adv. Energy Mater.* 12 (2022) 2103564.
- [28] B. Wang, C. Cheng, M. Jin, J. He, H. Zhang, W. Ren, J. Li, D. Wang, Y. Li, A site distance effect induced by reactant molecule matchup in single-atom catalysts for Fenton-like reactions, *Angew. Chem. Int. Ed.* 61 (2022), e202207268.
- [29] L. Li, K. Yuan, Y. Chen, Breaking the scaling relationship limit: from single-atom to dual-atom catalysts, *Acc. Mater. Res.* 3 (2022) 584–596.
- [30] Z. Zhao, M. Hu, T. Nie, W. Zhou, B. Pan, B. Xing, L. Zhu, Improved electronic structure from spin-state reconstruction of a heteronuclear Fe–Co diatomic pair to boost the fenton-like reaction, *Environ. Sci. Technol.* (2023).
- [31] J. Yang, D. Zeng, J. Li, L. Dong, W.-J. Ong, Y. He, A highly efficient Fenton-like catalyst based on isolated diatomic Fe–Co anchored on N-doped porous carbon, *Chem. Eng. J.* 404 (2021), 126376.
- [32] Z. Zhao, W. Zhou, D. Lin, L. Zhu, B. Xing, Z. Liu, Construction of dual active sites on diatomic metal (FeCo–N/C-x) catalysts for enhanced Fenton-like catalysis, *Appl. Catal. B: Environ.* 309 (2022), 121256.
- [33] B. Liu, H. Shioyama, T. Akita, Q. Xu, Metal-organic framework as a template for porous carbon synthesis, *J. Am. Chem. Soc.* 130 (2008) 5390–5391.
- [34] P. Hu, H. Su, Z. Chen, C. Yu, Q. Li, B. Zhou, P.J.J. Alvarez, M. Long, Selective degradation of organic pollutants using an efficient metal-free catalyst derived from carbonized polypyrrole via peroxymonosulfate activation, *Environ. Sci. Technol.* 51 (2017) 11288–11296.
- [35] K. Mamtani, D. Jain, D. Zemlyanov, G. Celik, J. Luthman, G. Renkes, A.C. Co, U. S. Ozkan, Probing the oxygen reduction reaction active sites over nitrogen-doped carbon nanostructures (CNx) in acidic media using phosphate anion, *ACS Catal.* 6 (2016) 7249–7259.
- [36] Y. Chen, S. Ji, Y. Wang, J. Dong, W. Chen, Z. Li, R. Shen, L. Zheng, Z. Zhuang, D. Wang, Y. Li, Isolated single iron atoms anchored on N-doped porous carbon as an efficient electrocatalyst for the oxygen reduction reaction, *Angew. Chem. Int. Ed.* 56 (2017) 6937–6941.
- [37] K. Qian, H. Chen, W. Li, Z. Ao, Y.-n. Wu, X. Guan, Single-atom Fe catalyst outperforms its homogeneous counterpart for activating peroxymonosulfate to achieve effective degradation of organic contaminants, *Environ. Sci. Technol.* 55 (2021) 7034–7043.
- [38] W.-D. Oh, Z. Dong, Z.-T. Hu, T.-T. Lim, A novel quasi-cubic CuFe₂O₄–Fe₂O₃ catalyst prepared at low temperature for enhanced oxidation of bisphenol A via peroxymonosulfate activation, *J. Mater. Chem. A* 3 (2015) 22208–22217.

- [39] W.-D. Oh, S.-K. Lua, Z. Dong, T.-T. Lim, High surface area DPA-hematite for efficient detoxification of bisphenol A via peroxymonosulfate activation, *J. Mater. Chem. A* 2 (2014) 15836–15845.
- [40] L. Hu, G. Zhang, Q. Wang, Y. Sun, M. Liu, P. Wang, Facile synthesis of novel $\text{Co}_3\text{O}_4\text{-Bi}_2\text{O}_3$ catalysts and their catalytic activity on bisphenol A by peroxymonosulfate activation, *Chem. Eng. J.* 326 (2017) 1095–1104.
- [41] G.-X. Huang, C.-Y. Wang, C.-W. Yang, P.-C. Guo, H.-Q. Yu, Degradation of bisphenol A by peroxymonosulfate catalytically activated with $\text{Mn}_{1.8}\text{Fe}_{1.2}\text{O}_4$ nanospheres: synergism between Mn and Fe, *Environ. Sci. Technol.* 51 (2017) 12611–12618.
- [42] X. Li, Z. Wang, B. Zhang, A.I. Rykov, M.A. Ahmed, J. Wang, $\text{Fe}_x\text{Co}_{3-x}\text{O}_4$ nanocages derived from nanoscale metal–organic frameworks for removal of bisphenol A by activation of peroxymonosulfate, *Appl. Catal. B: Environ.* 181 (2016) 788–799.
- [43] Y. Gao, Y. Zhu, L. Lyu, Q. Zeng, X. Xing, C. Hu, Electronic structure modulation of graphitic carbon nitride by oxygen doping for enhanced catalytic degradation of organic pollutants through peroxymonosulfate activation, *Environ. Sci. Technol.* 52 (2018) 14371–14380.
- [44] Y. Wang, D. Cao, M. Liu, X. Zhao, Insights into heterogeneous catalytic activation of peroxymonosulfate by $\text{Pd/g-C}_3\text{N}_4$: The role of superoxide radical and singlet oxygen, *Catal. Commun.* 102 (2017) 85–88.
- [45] Y. Wang, X. Zhao, D. Cao, Y. Wang, Y. Zhu, Peroxymonosulfate enhanced visible light photocatalytic degradation bisphenol A by single-atom dispersed Ag mesoporous $\text{g-C}_3\text{N}_4$ hybrid, *Appl. Catal. B: Environ.* 211 (2017) 79–88.
- [46] K.-Y.A. Lin, Z.-Y. Zhang, Degradation of Bisphenol A using peroxymonosulfate activated by one-step prepared sulfur-doped carbon nitride as a metal-free heterogeneous catalyst, *Chem. Eng. J.* 313 (2017) 1320–1327.
- [47] T. Yang, S. Fan, Y. Li, Q. Zhou, Fe-N/C single-atom catalysts with high density of Fe- N_x sites toward peroxymonosulfate activation for high-efficient oxidation of bisphenol A: electron-transfer mechanism, *Chem. Eng. J.* 419 (2021), 129590.
- [48] L.-S. Zhang, X.-H. Jiang, Z.-A. Zhong, L. Tian, Q. Sun, Y.-T. Cui, X. Lu, J.-P. Zou, S.-L. Luo, Carbon nitride supported high-loading Fe single-atom catalyst for activation of peroxymonosulfate to generate $^1\text{O}_2$ with 100% selectivity, *Angew. Chem. Int. Ed.* 60 (2021) 21751–21755.
- [49] X. Zhou, M.-K. Ke, G.-X. Huang, C. Chen, W. Chen, K. Liang, Y. Qu, J. Yang, Y. Wang, F. Li, H.-Q. Yu, Y. Wu, Identification of Fenton-like active Cu sites by heteroatom modulation of electronic density, *Proc. Natl. Acad. Sci.* 119 (2022), e2119492119.
- [50] C. Chu, J. Yang, X. Zhou, D. Huang, H. Qi, S. Weon, J. Li, M. Elimelech, A. Wang, J.-H. Kim, Cobalt single atoms on tetrapyrrolic macrocyclic support for efficient peroxymonosulfate activation, *Environ. Sci. Technol.* 55 (2021) 1242–1250.
- [51] Y. Qi, J. Li, Y. Zhang, Q. Cao, Y. Si, Z. Wu, M. Akram, X. Xu, Novel lignin-based single atom catalysts as peroxymonosulfate activator for pollutants degradation: role of single cobalt and electron transfer pathway, *Appl. Catal. B: Environ.* 286 (2021), 119910.
- [52] X. Li, X. Huang, S. Xi, S. Miao, J. Ding, W. Cai, S. Liu, X. Yang, H. Yang, J. Gao, J. Wang, Y. Huang, T. Zhang, B. Liu, Single cobalt atoms anchored on porous N-doped graphene with dual reaction sites for efficient fenton-like catalysis, *J. Am. Chem. Soc.* 140 (2018) 12469–12475.
- [53] N. Tian, X. Tian, Y. Nie, C. Yang, Z. Zhou, Y. Li, Biogenic manganese oxide: an efficient peroxymonosulfate activation catalyst for tetracycline and phenol degradation in water, *Chem. Eng. J.* 352 (2018) 469–476.
- [54] S. Liu, Z. Zhang, F. Huang, Y. Liu, L. Feng, J. Jiang, L. Zhang, F. Qi, C. Liu, Carbonized polyaniline activated peroxymonosulfate (PMS) for phenol degradation: role of PMS adsorption and singlet oxygen generation, *Appl. Catal. B: Environ.* 286 (2021), 119921.
- [55] X. Duan, H. Sun, Y. Wang, J. Kang, S. Wang, N-Doping-induced nonradical reaction on single-walled carbon nanotubes for catalytic phenol oxidation, *ACS Catal.* 5 (2015) 553–559.
- [56] I. Othman, J. Hisham Zain, M. Abu Haija, F. Banat, Catalytic activation of peroxymonosulfate using CeVO_4 for phenol degradation: an insight into the reaction pathway, *Appl. Catal. B: Environ.* 266 (2020), 118601.
- [57] Y. Yao, Z. Yang, H. Sun, S. Wang, Hydrothermal synthesis of Co_3O_4 -graphene for heterogeneous activation of peroxymonosulfate for decomposition of phenol, *Ind. Eng. Chem. Res.* 51 (2012) 14958–14965.
- [58] E. Saputra, S. Muhammad, H. Sun, S. Wang, Activated carbons as green and effective catalysts for generation of reactive radicals in degradation of aqueous phenol, *RSC Adv.* 3 (2013) 21905–21910.
- [59] L. Liu, C. Han, G. Ding, M. Yu, Y. Li, S. Liu, Y. Xie, J. Liu, Oxygen vacancies-enriched Cu/Co bimetallic oxides catalysts for high-efficiency peroxymonosulfate activation to degrade TC: Insight into the increase of Cu^+ triggered by Co doping, *Chem. Eng. J.* 450 (2022), 138302.
- [60] Y.-q. Wang, K. Li, M.-y. Shang, Y.-z. Zhang, Y. Zhang, B.-l. Li, Y.-j. Kan, X.-q. Cao, J. Zhang, A novel partially carbonized $\text{Fe}_3\text{O}_4\text{@PANI-p}$ catalyst for tetracycline degradation via peroxymonosulfate activation, *Chem. Eng. J.* 451 (2023), 138655.
- [61] J. Xie, X. Luo, L. Chen, X. Gong, L. Zhang, J. Tian, ZIF-8 derived boron, nitrogen co-doped porous carbon as metal-free peroxymonosulfate activator for tetracycline hydrochloride degradation: performance, mechanism and biotoxicity, *Chem. Eng. J.* 440 (2022), 135760.
- [62] X.-W. Zhang, M.-Y. Lan, F. Wang, C.-C. Wang, P. Wang, C. Ge, W. Liu, Immobilized N-C/Co derived from ZIF-67 as PS-AOP catalyst for effective tetracycline matrix elimination: from batch to continuous process, *Chem. Eng. J.* 450 (2022), 138082.
- [63] X.-q. Cao, F. Xiao, Z.-w. Lyu, X.-y. Xie, Z.-x. Zhang, X. Dong, J.-x. Wang, X.-j. Lyu, Y.-z. Zhang, Y. Liang, CuFe_2O_4 supported on montmorillonite to activate peroxymonosulfate for efficient ofloxacin degradation, *J. Water Process. Eng.* 44 (2021), 102359.
- [64] Y. Tian, Q. Li, M. Zhang, Y. Nie, X. Tian, C. Yang, Y. Li, pH-dependent oxidation mechanisms over FeCu doped $\text{g-C}_3\text{N}_4$ for ofloxacin degradation via the efficient peroxymonosulfate activation, *J. Clean. Prod.* 315 (2021), 128207.
- [65] T. Ni, Z. Yang, H. Zhang, L. Zhou, W. Guo, L. Pan, Z. Yang, K. Chang, C. Ge, D. Liu, Peroxymonosulfate activation by $\text{Co}_3\text{O}_4\text{/SnO}_2$ for efficient degradation of ofloxacin under visible light, *J. Colloid Interface Sci.* 615 (2022) 650–662.
- [66] X. Li, Z. Ye, S. Xie, H. Li, Y. Lv, Y. Wang, Y. Wang, C. Lin, Insight into the performance and mechanism of peroxymonosulfate activation by B, N co-doped hierarchical porous carbon for phenol degradation, *J. Environ. Chem. Eng.* 10 (2022), 108264.
- [67] F. Xiao, Y.-q. Wang, X.-y. Xie, X. Dong, Y.-j. Kan, Y. Zhang, Y.-z. Zhang, G. Zhou, B.-l. Li, X.-q. Cao, J. Zhang, M. Chen, L. Li, X.-j. Lyu, Preparation of Fe/C-Mt composite catalyst and ofloxacin removal by peroxymonosulfate activation, *Sep. Purif. Technol.* 298 (2022), 121548.
- [68] C. Huang, Y. Wang, M. Gong, W. Wang, Y. Mu, Z.-H. Hu, $\alpha\text{-MnO}_2\text{/Palygorskite}$ composite as an effective catalyst for heterogeneous activation of peroxymonosulfate (PMS) for the degradation of Rhodamine B, *Sep. Purif. Technol.* 230 (2020), 115877.
- [69] S. Kang, J. Hwang, CoMn_2O_4 embedded hollow activated carbon nanofibers as a novel peroxymonosulfate activator, *Chem. Eng. J.* 406 (2021), 127158.
- [70] W. Ma, Y. Du, N. Wang, P. Miao, ZIF-8 derived nitrogen-doped porous carbon as metal-free catalyst of peroxymonosulfate activation, *Environ. Sci. Pollut. Res.* 24 (2017) 16276–16288.
- [71] S. Wang, Y. Liu, J. Wang, Peroxymonosulfate Activation by Fe-Co-O-Codoped Graphite Carbon Nitride for Degradation of Sulfamethoxazole, *Environ. Sci. Technol.* 54 (2020) 10361–10369.
- [72] Y. Xue, Z. Wang, R. Naidu, R. Bush, F. Yang, J. Liu, M. Huang, Role of halide ions on organic pollutants degradation by peroxysensitized advanced oxidation processes: a critical review, *Chem. Eng. J.* 433 (2022), 134546.
- [73] R. Luo, M. Li, C. Wang, M. Zhang, M.A. Nasir Khan, X. Sun, J. Shen, W. Han, L. Wang, J. Li, Singlet oxygen-dominated non-radical oxidation process for efficient degradation of bisphenol A under high salinity condition, *Water Res.* 148 (2019) 416–424.
- [74] Y. Zhou, J. Hu, Z. Zeng, J. Fu, Y. Gao, B. Han, Y. Song, Y. Luo, J. Jiang, Oxidative removal of dissolved manganese(II) by peroxymonosulfate: non-radical mechanism and influencing factors, *Chem. Eng. J.* 454 (2023), 140108.
- [75] F. Wang, H. Fu, F.-X. Wang, X.-W. Zhang, P. Wang, C. Zhao, C.-C. Wang, Enhanced catalytic sulfamethoxazole degradation via peroxymonosulfate activation over amorphous $\text{CoS}_x\text{@SiO}_2$ nanocages derived from ZIF-67, *J. Hazard Mater.* 423 (2022), 126998.
- [76] Y. Gao, X.-H. Yi, C.-C. Wang, F. Wang, P. Wang, Effective, Cr(VI) reduction over high throughput Bi-BDC MOF photocatalyst, *Mater. Res. Bull.* 158 (2023), 112072.
- [77] Z.-Y. Guo, Y. Si, W.-Q. Xia, F. Wang, H.-Q. Liu, C. Yang, W.-J. Zhang, W.-W. Li, Electron delocalization triggers nonradical Fenton-like catalysis over spinel oxides, *Proc. Natl. Acad. Sci.* 119 (2022), e2201607119.
- [78] Y. Zhou, J. Jiang, Y. Gao, J. Ma, S.-Y. Pang, J. Li, X.-T. Lu, L.-P. Yuan, Activation of peroxymonosulfate by benzoquinone: a novel nonradical oxidation process, *Environ. Sci. Technol.* 49 (2015) 12941–12950.
- [79] P. Shao, J. Tian, F. Yang, X. Duan, S. Gao, W. Shi, X. Luo, F. Cui, S. Luo, S. Wang, Identification and regulation of active sites on nanodiamonds: establishing a highly efficient catalytic system for oxidation of organic contaminants, *Adv. Funct. Mater.* 28 (2018) 1705295.
- [80] J. Li, Y. Wan, Y. Li, G. Yao, B. Lai, Surface Fe(III)/Fe(II) cycle promoted the degradation of atrazine by peroxymonosulfate activation in the presence of hydroxylamine, *Appl. Catal. B: Environ.* 256 (2019), 117782.
- [81] Y.-L. He, C.-S. He, L.-D. Lai, P. Zhou, H. Zhang, L.-L. Li, Z.-K. Xiong, Y. Mu, Z.-C. Pan, G. Yao, B. Lai, Activating peroxymonosulfate by N and O co-doped porous carbon for efficient BPA degradation: a re-visit to the removal mechanism and the effects of surface unpaired electrons, *Appl. Catal. B: Environ.* 314 (2022), 121390.
- [82] F. Wang, Y. Gao, H. Chu, Y. Wei, C.-C. Wang, S.-S. Liu, G. Liu, H. Fu, P. Wang, C. Zhao, The pivotal role of selenium vacancies in defective $\text{FeSe}_2\text{@MoO}_3$ for efficient peroxymonosulfate activation: experimental and DFT calculation, *ACS EST Engg* (2023), <https://doi.org/10.1021/acsestengg.3c00195>.
- [83] J. Miao, Y. Zhu, J. Lang, J. Zhang, S. Cheng, B. Zhou, L. Zhang, P.J.J. Alvarez, M. Long, Spin-state-dependent peroxymonosulfate activation of single-atom M-N moieties via a radical-free pathway, *ACS Catal.* 11 (2021) 9569–9577.
- [84] Y. Chen, G. Zhang, H. Liu, J. Qu, Confining free radicals in close vicinity to contaminants enables ultrafast Fenton-like processes in the interspersing of MoS_2 membranes, *Angew. Chem. Int. Ed.* 58 (2019) 8134–8138.
- [85] W. Ren, G. Nie, P. Zhou, H. Zhang, X. Duan, S. Wang, The intrinsic nature of persulfate activation and N-doping in carbocatalysis, *Environ. Sci. Technol.* 54 (2020) 6438–6447.
- [86] P. Huang, P. Zhang, C. Wang, J. Tang, H. Sun, Enhancement of persulfate activation by Fe-biochar composites: synergism of Fe and N-doped biochar, *Appl. Catal. B: Environ.* 303 (2022), 120926.
- [87] C. Zhao, L. Meng, H. Chu, J.-F. Wang, T. Wang, Y. Ma, C.-C. Wang, Ultrafast degradation of emerging organic pollutants via activation of peroxymonosulfate over $\text{Fe}_3\text{C/Fe@N-C-x}$: Singlet oxygen evolution and electron-transfer mechanisms, *Appl. Catal. B: Environ.* 321 (2023), 122034.
- [88] M. Zhang, R. Luo, C. Wang, W. Zhang, X. Yan, X. Sun, L. Wang, J. Li, Confined pyrolysis of metal–organic frameworks to N-doped hierarchical carbon for non-radical dominated advanced oxidation processes, *J. Mater. Chem. A* 7 (2019) 12547–12555.
- [89] X. Duan, Z. Ao, H. Sun, L. Zhou, G. Wang, S. Wang, Insights into N-doping in single-walled carbon nanotubes for enhanced activation of superoxides: a mechanistic study, *Chem. Commun.* 51 (2015) 15249–15252.